Journal of Advances in Modeling Earth Systems

RESEARCH ARTICLE
10.1029/2018MS001382

Radiatively Induced Precipitation Formation in Diamond Dust

Xiping Zeng[1]

[1]Atmospheric Modeling Branch, U.S. Army Research Laboratory, Adelphi, MD, USA

Key Points:
- A numerical model of diamond dust is developed to simulate the effect of radiative cooling on ice crystal size and shape in diamond dust
- The model shows that radiative cooling can bring about low ice crystal concentration via precipitation formation in stationary air
- The model is supported by the lidar-beam reflection observations over Greenland that large ice crystals grow whereas small ones sublimate

Abstract Radiative cooling leads to the formation of dew and frost. This process is extended into a numerical model to simulate the ice crystal characteristics of diamond dust. The model replicates the low ice crystal concentration of diamond dust and the precipitation in stationary air. Its results are consistent with the arctic observations that large ice crystals grow while small ones sublimate and partly explain the geographic and seasonal distributions of diamond dust such as the high frequency of diamond dust in the arctic regions and winter. Furthermore, its results show that plate/column-like ice crystals with radiative cooling grow in expense of quasi-spherical ice particles, partly explaining the ice crystal shapes observed in diamond dust.

Correspondence to:
X. Zeng,
xiping.zeng.civ@mail.mil

Citation:
Zeng, X. (2018). Radiatively induced precipitation formation in diamond dust. *Journal of Advances in Modeling Earth Systems*, *10*, 2300–2317. https://doi.org/10.1029/2018MS001382

Received 21 MAY 2018
Accepted 25 AUG 2018
Accepted article online 3 SEP 2018
Published online 22 SEP 2018

1. Introduction

1.1. Motivation

How ice clouds precipitate is a challenging topic in meteorology (see Gultepe et al., 2017, for review). Ice clouds are not represented well in the current climate models and vary greatly from one model to another (e.g., Girard & Blanchet, 2001a; Jiang et al., 2012; Klein et al., 2009; Ricaud et al., 2017; Zhang et al., 2001). Their modeling problem exists in high-resolution models, too. Cloud-resolving models, for example, usually generate excessively thick (or insufficiently thin) cloud anvils (e.g., Powell et al., 2012; Zeng et al., 2013). Furthermore, operational models can capture thicker cloud layers over Antarctica but have substantial difficulty reproducing very thin diamond dust layers (Ricaud et al., 2017). This modeling problem could be due to a lack of accurate microphysics.

If there is a precipitation process that converts thick clouds to thin ones, the problem may be solved or alleviated. Diamond dust (or clear-sky ice crystal precipitation) provides one example of a precipitation process that can address this problem, which motivates this study.

Diamond dust is common in the arctic regions. Its characteristics are described in the World Meteorological Organization (https://cloudatlas.wmo.int/diamond-dust.html) terminology as the following:

> "Diamond dust can be observed in polar and alpine regions and continental interiors, especially in clear, calm and cold weather. It forms at temperatures typically less than −10 °C in a rapidly cooling airmass. Diamond dust is usually composed of well-developed crystals (often plates)."

In addition, "visibility in diamond dust varies considerably, and its lower limit is greater than 1 km."

Since visibility depends on both ice crystal concentration (ICC) and ice crystal size, it is ambiguous to classify diamond dust from ice fog via visibility. Even so, the frequency of diamond dust is estimated to be about 20–50% in the arctic regions during wintertime (e.g., Curry et al., 1996; Gultepe, 2015; Gultepe et al., 2018; Walden et al., 2003). In addition, the frequency of diamond dust varies considerably from region to region and season to season. Observations of ground-based and space-borne lidars and cloud radars revealed diamond dust is frequent in late winter and early spring in the high latitudes (e.g., Intrieri & Shupe, 2004; Liu et al., 2012).

Vertical mixing within the planetary boundary layer as well as the radiative cooling snow surface was used to explain the formation of diamond dust, which can bring about the boundary layer air supersaturated with respect to ice (Curry et al., 1996; van As & van den Broeke, 2006). Once the air becomes supersaturated with respect to ice, the ice nucleation theory (e.g., Pruppacher & Klett, 1997) predicts that active ice nuclei and subsequently formed ice crystals therein would possess high number concentrations. However, the ICC of diamond dust is quite low (e.g., ~20 L^{-1}; Kikuchi & Hogan, 1979). Hence, a further question is how to

understand the low ICC and other ice crystal characteristics in diamond dust (e.g., Goerke et al., 2017; Kikuchi & Hogan, 1979; Santachiara et al., 2017; Walden et al., 2003).

1.2. Radiative Effect on Microphysics

As another thread, radiation impacts liquid drop (or ice crystal) growth via changing drop (or ice crystal) temperature. Its effect on microphysics, referred to here as radiative effect on microphysics (REM), is well known because it brings about dew/frost via the radiative cooling of dewdrops/frost (and their supporters, e.g., grass leaves; e.g., Koeppe & De Long, 1958).

However, the studies of REM progressed slowly due to the complication of cloud microphysics and radiation. Fuchs (1959) considered droplets embedded inside an optically thick cloud layer by treating liquid drops and the atmosphere as blackbodies and then concluded REM is negligible there, overlooking cloud boundaries and optically thin clouds. After taking account of the quasi-transparent regions within the atmospheric radiative spectrum (also known as atmospheric windows), the pioneering studies of REM revealed the importance of REM near cloud boundaries and in optically thin clouds (e.g., Barkstrom, 1978; Heymsfield, 1973; Roach, 1976; Stephens, 1983). Stephens (1983) further put forward a good treatment of radiation on ice crystals, especially on the dependence of crystal emissivity (or absorptivity) on crystal size. Since then, REM was implemented into numerical models to assess its contribution to drop (or ice crystal) growth (e.g., Ackerman et al., 1995; Austin et al., 1995; Bott et al., 1990; Guzzi & Rizzi, 1980; Hall & Pruppacher, 1976; Harrington et al., 2000; Lebo et al., 2008; Roach, 1976; Wu et al., 2000; Zeng, 2008, 2018a).

REM performs differently when ice crystals undergo different radiative cooling/warming. As a result, its performance varies with clouds and even cloud regions (e.g., Stephens, 1983; Wu et al., 2000; Zeng, 2008). The performance is classified with the aid of an analytical expression of REM that uses a radiative ratio η_z to describe the radiative environment of REM (Zeng, 2008; also see equation (12) for further discussions). When $\eta_z <$(or $>$) 1, ice crystals undergo radiative cooling (or warming), and consequently REM broadens (or narrows) ice crystal spectrum. Hence, $\eta_z - 1$ or its distribution can be used to predict the geographical and seasonal distributions of REM (e.g., Zeng, 2008, 2018ab; also see section 4.1).

1.3. REM Observations and Diamond Dust

REM originates in daily observations of dew and frost. Its spectrum broadening effect was duplicated in a laboratory experiment of Brewster and McNichols (2018) in a radiative cooling environment. A further question is whether observational data support the existence of REM in clouds aloft.

Since REM's performance varies greatly with clouds and/or cloud regions, REM's performance needs a classification first and then observational data are used to assess REM. Zeng (2008) showed that REM has the same performance for a given radiative environment (i.e., a given η_z). Hence, an assessment of REM consists of two steps: sorting observational data based on the magnitude of $\eta_z - 1$ (or other similar variables) first and then comparing the observational data with REM's prediction (or modeling).

Four assessments of REM have been carried out against observations. The first assessment was applied to warm clouds (Zeng, 2018a), showing that the REM modeling is consistent with the Rain In shallow Cumulus over the Ocean observations of drop spectrum (Small & Chuang, 2008) and the Tropical Rainfall Measuring Mission satellite observations of warm rain (Liu & Zipser, 2009). The second assessment was applied to the arctic regions where η_z is usually less than one (see section 4.1), addressing the formation of diamond dust. The third assessment was applied to thick-cloud top from the low to high latitudes (Gong et al., 2018; Zeng et al., 2016), using the polarization difference data of Global Precipitation Measurement Microwave Imager (Skofronick-Jackson et al., 2008, 2015). The fourth assessment was applied to the tropical upper troposphere (Zeng, 2018b), showing the consistency between the CloudSat observations of thin clouds and the prediction of REM-induced precipitation (Zeng, 2008).

This paper presents the second assessment, addressing a connection between REM and diamond dust. The paper consists of five sections. Section 2 introduces REM in a numerical model. Section 3 carries out numerical simulations to show how radiative cooling brings about precipitation. Section 4 compares model results with diamond dust observations. Section 5 gives a summary. Except for special illustrations, all symbols are defined in Appendix B.

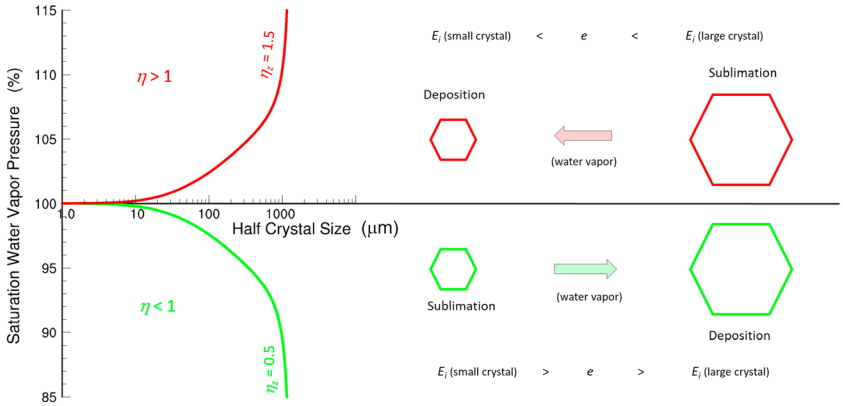

Figure 1. Schematic diagram of radiative effect on microphysics for two adjacent ice crystals. Saturation water vapor pressure around an ice crystal E_i varies with half crystal size a; red and green lines denote E_i with $\eta > 1$ (radiative warming) and $\eta < 1$ (radiative cooling), respectively. Arrow indicates the direction of water vapor diffusion between two ice crystals. When $\eta < 1$, the water vapor pressure e is lower (or higher) than E_i of the smaller (or larger) crystal. As a result, the smaller crystal sublimates with the resulting water vapor depositing on and therefore increasing the size of the larger crystal. Quantitatively, the vertical axis represents E_i with radiative cooling/warming normalized by that without radiation (or the critical relative humidity in equation (10)). Red and green lines are obtained for plate-like ice crystals at $T = -30$ °C and $p = 680$ hPa using $\eta_z = 1.5$ and 0.5, respectively.

2. Representing the REM

2.1. Processes on Radiation and Cloud Microphysics

Radiation impacts the ice crystal temperature that, in turn, affects the saturation water vapor pressure around ice crystals and eventually alters the diffusional growth rate of crystals (e.g., Hall & Pruppacher, 1976; Heymsfield, 1973; Roach, 1976; Stephens, 1983; Wu et al., 2000; Zeng, 2008). When radiation cools ice crystals, it brings about precipitating ice crystals in ice clouds just as frost forms (Zeng, 2008). When radiation warms ice crystals, large ice crystals shrink via sublimation (Wu et al., 2000; Zeng, 2008). Such different effects of radiation on microphysics (or REM) are discussed mathematically below for three cases, beginning with REM for a single ice crystal.

1. For a single ice crystal of mass m, a radiative ratio η for the ice crystal is defined as (Zeng, 2008)

$$\eta = \frac{\text{infrared flux incident on ice crystal surface}}{\sigma T^4 S}, \tag{1}$$

where σ is the Stefan-Boltzmann constant; T, the environmental air temperature; and S, the surface area of ice crystal. Since the surface temperature of ice crystal $T_s = T + \Delta T$ (where ΔT is the difference in temperature

Table 1
Properties of Individual Ice Crystals

Crystal shape	Sphere	Prolate spheroid	Oblate spheroid
Parameters	Radius: r	Semimajor length: a Seminor length: b	Semimajor length: a Seminor length: b
Surface area S	$4\pi r^2$	$2\pi b\left(b + \frac{a^2}{\sqrt{a^2-b^2}} \arcsin\frac{\sqrt{a^2-b^2}}{a}\right)$	$2\pi a\left(a + \frac{b^2}{\sqrt{a^2-b^2}} \ln\frac{\sqrt{a^2-b^2}+a}{b}\right)$
Shape factor C	r	$\frac{\sqrt{a^2-b^2}}{\ln\left[\left(a+\sqrt{a^2-b^2}\right)/b\right]}$	$\frac{\sqrt{a^2-b^2}}{\arcsin\sqrt{1-b^2/a^2}}$
Relation of η to η_z	$\eta - 1 = \frac{1}{2}(\eta_z - 1)$	$\eta - 1 = \frac{2\pi a^2}{S}(\eta_z - 1)$ (horizontal) $\eta - 1 = \frac{2\pi ab}{S}(\eta_z - 1)$ (vertical)	$\eta - 1 = \frac{2\pi ab}{S}(\eta_z - 1)$ (horizontal) $\eta - 1 = \frac{2\pi b^2}{S}(\eta_z - 1)$ (vertical)
Real ice crystals	Rosette crystals, Equidimensional	Column-like crystals, Bullet-shaped crystals	Plate-like crystals

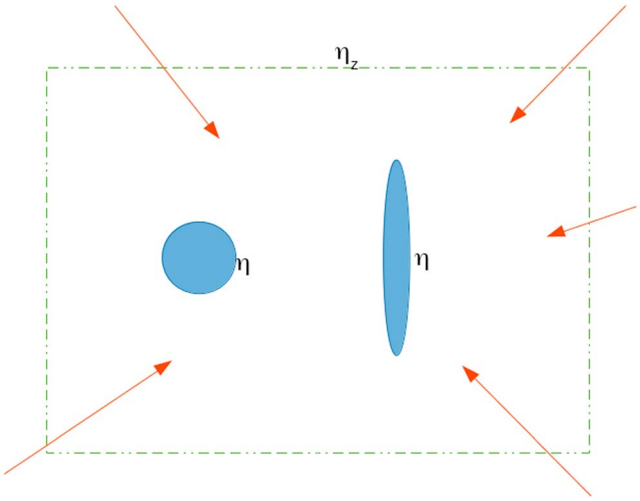

Figure 2. Vertical cross section of an air parcel (enclosed by the green line) with spherical and column-like ice crystals embedded (blue). Red arrows represent radiation into the parcel. The air parcel (or layer) is described by η_z, whereas each ice crystal by its own η.

between ice crystal and its environmental air) and $\Delta T/T \ll 1$, the ice crystal emits infrared radiation outward with an energy flux of $\varepsilon_0\sigma T_s^4$, which is expanded in Taylor's series of $\Delta T/T$, becoming

$$\varepsilon_0\sigma T_s^4 \approx \varepsilon_0\sigma T^4 + 4\varepsilon_0\sigma T^3\Delta T, \tag{2}$$

where ε_0 denotes the emissivity (or bulk absorption efficiency) of ice crystal for blackbody radiation. Since ε_0 is close to 1 for large ice crystals (see section 2.3 for the expression of ε_0) and $\Delta T/T \ll 1$, thus, σT^4 is very close to $\varepsilon_0\sigma T_s^4$. Hence, η approximately represents the ratio of the inward radiative flux to the outward one at the crystal surface, and therefore, $\eta - 1$ can be used to measure the infrared radiation cooling (or warming) of an ice crystal approximately. When $\eta = 1$ (neither radiative cooling nor warming), the ice crystal grows just as predicted by the classic theory of cloud physics without REM (Fuchs, 1959; Mason, 1957; Rogers & Yau, 1989).

If the atmosphere were a blackbody, $\eta \approx 1$. In fact, the atmosphere has quasi-transparent regions within the radiative spectrum (or atmospheric windows) and thus is not a blackbody (e.g., Stephens, 1983). Hence, η usually deviates from 1. As a result, radiation alters the ice crystal temperature and subsequently the saturation water vapor pressure around crystals. An analytical expression of ice crystal growth rate as well as ΔT is derived as a function of η_z (Zeng, 2008).

Figure 1 illustrates the saturation water vapor pressure E_i against ice crystal size for $\eta > 1$ (radiative warming) and $\eta < 1$ (radiative cooling), respectively. The dependence of E_i (or ΔT) on crystal size originates in the different sensitivities of the radiative and conductive energy fluxes at crystal surface to crystal size (e.g., Lebo et al., 2008; Zeng, 2008). For a spherical ice crystal of radius r, for example, the radiative emission rate at crystal surface is directly proportional to r^2 (or crystal surface area), whereas the conductive energy transfer rate is proportional to r (or crystal size) only. Specifically, the dependence of ice crystal temperature on size is illustrated with a spherical ice crystal of radius r that involves only radiative and conductive heat transfers. The radiative energy transfer from the crystal to its environment $Q_r \propto r^2(1-\eta)$ and the heat conduction from the environment to the crystal $Q_c \propto r(T - T_s)$, where T_s is ice crystal temperature. When the crystal stays at its steady state, $Q_r = Q_c$. As a result, $T - T_s \propto r(1-\eta)$, which shows that ice crystal temperature decreases (or increases) with increasing r when $\eta < 1$ (or > 1).

When $\eta < 1$ (radiative cooling), E_i decreases with increasing crystal size. Hence, an ice crystal can grow in a subsaturated environment, reaching hundreds of micrometers (see section 3.1 for modeling). This growth mechanism resembles the formation of frost in a subsaturated environment, if frost and its supporter (e.g., grass leaf) are treated together as one body for heat balance.

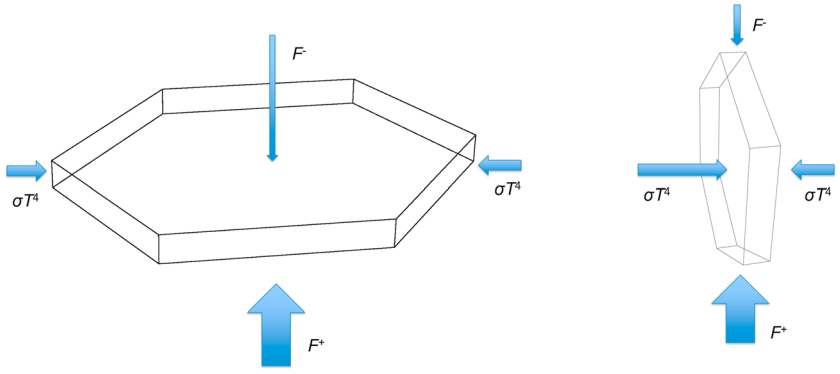

Figure 3. Schematic diagrams of horizontally (left) and vertically oriented (right) plate-like crystals receiving upward (F^+), downward (F^-), and horizontal infrared radiation ($\sim\sigma T^4$). Since F^+ and F^- usually deviate from σT^4, horizontally and vertically oriented crystals have different energy budgets and therefore different ice crystal temperatures.

Table 2
List of the Numerical Experiments

Experiment	Crystal shape (orientation)	w_{eff}	Notes
Ph	+Plate (horizontal)	0	Selection of large ice crystals (default experiment)
PhPv	+Plate (horizontal) +Plate (vertical)	0	Effect of crystal orientation
ChCv	+Column (horizontal) +Column (vertical)	0	
PhS	+Plate (horizontal) +Spherical solid crystals	0	Selection of crystal shape
PhCh	+Plate (horizontal) +Column (horizontal)	0	
PhPvW	+Plate (horizontal) +Plate (vertical)	1 cm/s	Effect of vertical velocity
PhF	+Plate (horizontal)	0	Some large ice crystals falling out

2. Consider REM for two adjacent ice crystals (shown in Figure 1). When $\eta > 1$ (red lines), the larger crystal has a higher temperature and subsequently larger saturation water vapor pressure around it. As a result, the larger crystal sublimates with the resulting water vapor being deposited onto the smaller one (Wu et al., 2000; Zeng, 2008). In contrast, when $\eta < 1$ (green lines), the smaller crystal has a higher temperature and subsequently larger saturation water vapor pressure around it. As a result, the smaller crystal sublimates with the resulting water vapor being deposited onto the larger one, which serves as a potential precipitation generation mechanism (Zeng, 2008).
3. Consider multiple ice crystals that coexist in an air parcel. They compete for available water vapor and REM alters their competition for water vapor. As a result, REM brings about a nonlinear evolution of ice crystal spectrum. Zeng (2008) developed a bin (or particle size-resolving) model to simulate how REM modulates ice crystal size for a given ice crystal shape. In this paper, the model is extended to include both ice crystal shape and orientation.

2.2. Representing Ice Crystal Shapes

Consider an air parcel that contains multiple ice crystals and moves with a vertical velocity of w (by assuming the air is horizontally uniform). Its tendency of relative humidity with respect to ice H_i, based on the conservation of energy and water, is derived as (see Appendix A)

$$\frac{dH_i}{dt} = Q_1(T)w_{eff} - Q_2(T)\sum_{j,k}\frac{dm_{jk}}{dt}, \tag{3}$$

where m_{jk} ($j = 1, 2, \ldots$) denotes the mass of differently sized ice crystals for a given crystal shape k, and the effective vertical velocity is defined as

$$w_{eff} = w + \frac{Q_3(T)}{Q_1(T)}. \tag{4}$$

The expressions of Q_1, Q_2, and Q_3 in (3) and (4) are given in Appendix A. In short, the terms of dH_i/dt and Q_2 in (3) represent the competition of ice crystals for available water vapor, and the term of Q_1 represents the effect of air temperature on H_i via vertical velocity w and the radiative cooling/warming term of air Q_3.

All ice crystals are classified into five shapes (or $k = 1$ to $k = 5$; see Table 1 for their properties): Shape 1, a sphere of radius r and surface area $S = 4\pi r^2$ for equidimensional and rosette crystals; Shape 2, a prolate spheroid of semimajor and minor axis lengths a and b for column-like crystals whose surface area is

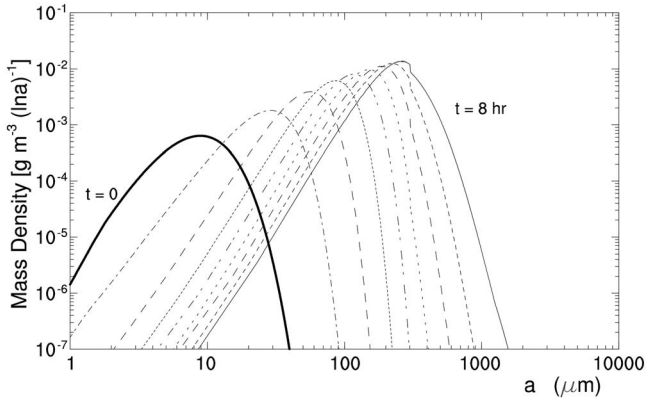

Figure 4. Evolution of mass density dM (ln$a$)/dln$a$ versus half crystal size a in experiment Ph for horizontally oriented plate crystals assuming the following parameter values: $w_{eff} = 0$, $\eta_z = 0.5$, $T = -30$ °C, and $p = 680$ hpa. Thick line denotes initial spectrum; time interval between lines is 1 hr.

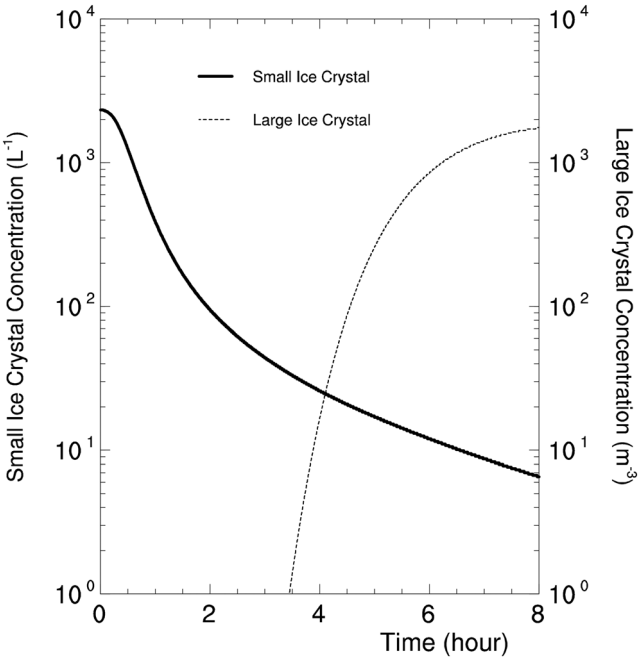

Figure 5. Concentrations of small ice crystals whose half crystal size a is between 1 and 200 μm (solid line) and large (or precipitating) ones whose half crystal size is longer than 200 μm (dashed line) versus time in experiment Ph.

$$S = 2\pi b\left(b + \frac{a^2}{\sqrt{a^2 - b^2}}\arcsin\frac{\sqrt{a^2 - b^2}}{a}\right); \tag{5}$$

Shape 3, an oblate spheroid of semimajor and minor axis lengths a and b for plate-like crystals, for which

$$S = 2\pi a\left(a + \frac{b^2}{\sqrt{a^2 - b^2}}\ln\frac{\sqrt{a^2 - b^2} + a}{b}\right); \tag{6}$$

Shape 4, a prolate spheroid for bullet-shaped crystals; and Shape 5, a sphere for rosette crystals that consist of bullets. All of the crystal shapes have their own formulas of ice crystal mass, terminal velocity, dimensional relationship, and ventilation factors against crystal size. The formulas are empirically obtained from field observations (e.g., Auer & Veal, 1970; Heymsfield, 1972; Heymsfield & Iaquinta, 2000; see Zeng, 2008 for computational details).

2.3. Computing η

The analytic expression of ice crystal growth rate was derived as a function of η (Zeng, 2008), using equation (2) and an approximate expression of ΔT that was obtained from the Clausius-Clapeyron equation by Mason (1957, p. 109). The growth rate of an ice crystal or dm/dt in equation (3) is rewritten, after some algebraic operations and approximation, as

$$\frac{dm}{dt} = \frac{4\pi C(H_i - 1)}{H_{ic}A + B} + \frac{S\varepsilon_0\sigma T^3}{KF_\alpha f_Q(H_{ic}A + B)}\left(\frac{L_s}{R_vT} - 1\right)\left(1 - \varepsilon_r\eta - \frac{F_s}{\varepsilon_0\sigma T^4}\right), \tag{7}$$

where C is the stationary diffusion shape factor that accounts for the influence of crystal shape on water vapor field around an ice crystal or the electrostatic capacity of a conductor whose size and shape are the same as those of the ice crystal (for a spherical crystal of radius r, $C = r$; McDonald, 1963), η describes the infrared radiation received by the ice crystal, F_s represents the solar radiation absorbed by the ice crystal,

$$A = \frac{L_s}{F_\alpha f_Q KT}\left(\frac{L_s}{R_vT} - 1\right), \tag{8}$$

$$B = \frac{R_vT}{F_\beta f_m DE_i(T)}, \tag{9}$$

and the critical relative humidity (or the saturation water vapor pressure around an ice crystal with radiative cooling/warming normalized by that around the same ice crystal without radiation)

$$H_{ic} = 1 - \left(\frac{L_s}{R_vT} - 1\right)\left(1 - \varepsilon_r\eta - \frac{F_s}{\varepsilon_0\sigma T^4}\right)\frac{S\varepsilon_0\sigma T^3}{4\pi CKF_\alpha f_Q} \tag{10}$$

(see Appendix B for the other symbol definitions).

To be specific, the concise expression of ice crystal growth rate or equation (7), in comparison to the original one or equation (24) of Zeng (2008), is derived with two approximations in the denominator of (7): (a) The ratio between the infrared-radiation flux and the conductive heat flux from air to an ice crystal χ is proportional to S/C and, thus, is quite small for small ice crystals. Its major effect on REM is represented explicitly in the numerator of (7), whereas its minor effect on A in the denominator of (7) is neglected; that is, $(1 + \chi)A \approx A$ in the denominator of (7). (b) The relative change in ice crystal temperature due to radiation γ is much smaller than 1. Thus, its major effect on REM is represented explicitly in the numerator of (7), whereas its minor effect is neglected or $(1 - \gamma)^2 \approx 1$ is used in the denominator of (7).

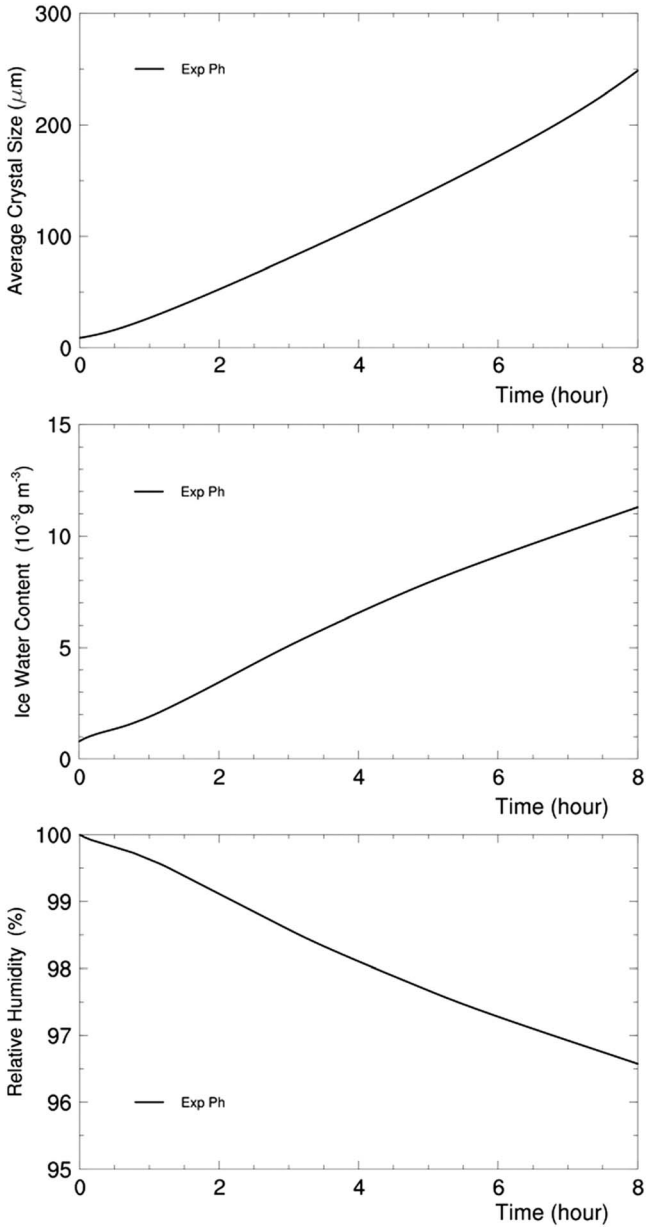

Figure 6. Time series of average half crystal size a (top), ice water content (middle), and relative humidity with respect to ice (bottom) in experiment Ph.

Since the absorption length (mean-free path of a photon before absorption) is 19 μm at wavelength 9 and 850 μm at wavelength 23 μm (Warren & Brandt, 2008) and the crystals are often smaller than the absorption length, the bulk absorption efficiency (or emissivity) of an ice crystal for blackbody radiation varies with ice crystal size. In the present simulations, it takes

$$\varepsilon_0 = 0.9\{1 - \exp[-Tr^*/(T_{\text{ref}} r_{\text{ref}})]\} \tag{11}$$

to represent its dependence on ice crystal size, where the equivalent radius of an ice crystal $r^* = S/4\pi C$ and the reference constants $T_{\text{ref}} = 261$ K and $r_{\text{ref}} = 6$ μm (Stephens, 1983; Zeng, 2008).

The ratio η in (7) is determined, using F^+ and F^- that are the upward and downward fluxes of infrared radiation in the atmosphere, respectively. A radiative ratio for an air parcel is defined as (Zeng, 2008)

$$\eta_z = \frac{F^+ + F^-}{2\sigma T^4}. \tag{12}$$

Once atmospheric variables are known, η_z can be obtained easily by using a two-stream radiation package to calculate F^+ and F^- (e.g., Chou et al., 1995; Fu & Liou, 1992).

The relationship of η to η_z is listed in Table 1 and illustrated graphically in Figure 2. For a given air parcel (exactly an air layer in Figure 2), only one η_z is used to describe the inward radiative flux through parcel boundary. Since η_z is normalized by a scale of energy flux σT^4 or the blackbody irradiance at temperature T, $\eta_z - 1$ can be used to measure the warming (or cooling) of an air parcel approximately.

The sign of $\eta_z - 1$ is discussed from the introduction of (12). Consider a horizontally oriented plate ice crystal whose depth is quite small. It absorbs infrared radiation by $a_0 A(F^+ + F^-)$, where a_0 is the absorptivity of the ice crystal and A the maximum horizontal cross-sectional area. Meanwhile, it emits infrared radiation by $2\varepsilon_0 A\sigma T^4$, where ε_0 denotes emissivity of the ice crystal and σT^4 the blackbody irradiance at temperature T. Thus, the ratio of absorbed infrared radiation energy to emitted radiation energy is expressed as

$$\eta_z = \frac{a_0}{\varepsilon_0}\frac{F^+ + F^-}{2\sigma T^4}.$$

Since Kirchhoff's law shows $a_0 = \varepsilon_0$, the preceding equation degenerates into (12). Similarly, consider an air layer that is quite thin but thick enough to host many ice crystals (or Figure 2). Its ratio of absorbed infrared radiation to emitted radiation is also expressed by the preceding equation except that a_0 and ε_0 denote the absorptivity and emissivity of the air layer, respectively. The preceding equation degenerates into (12) too because $a_0 = \varepsilon_0$. Hence, the preceding equation suggests that positive (or negative) sign of $\eta_z - 1$ indicates warming (or cooling) of an air parcel.

Let us return to the relationship of η to η_z. For a given air parcel with multiple ice crystals embedded, there are multiple η for individual ice crystals and η varies with ice crystal characteristics (e.g., shape and orientation). The relationship of η to η_z is determined below with the aid of Figure 3.

Consider an ice crystal that receives the upward radiation (F^+), downward radiation (F^-), and horizontal radiation ($\approx\sigma T^4$). Since the atmosphere is not a blackbody, the upward infrared flux F^+ and downward one F^- usually deviate from the horizontal one (or σT^4). Their contribution to an ice crystal is approximated with $(F^+ + F^-)$ times the maximum horizontal cross-sectional area of the crystal, which depends on ice crystal shape and orientation.

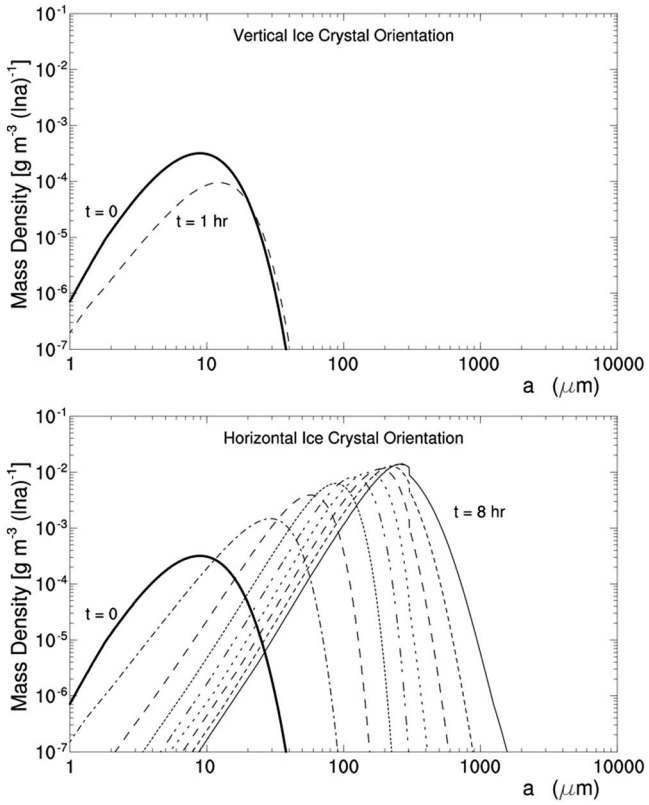

Figure 7. Evolution of mass density dM (ln$a$)/dln$a$ versus half crystal size a in experiment PhPv for vertically (top) and horizontally oriented (bottom) plate crystals. Thick lines denote initial spectra; time interval between lines is 1 hr.

A horizontally oriented plate-like ice crystal is discussed first. It is mimicked by an oblate spheroid of semimajor and minor axis lengths a and b (McDonald, 1963). Since its maximum horizontal cross-sectional area is πa^2, the spheroid receives the upward and downward infrared fluxes $\pi a^2 F^+$ and $\pi a^2 F^-$, respectively, whereas the crystal with the remaining surface area of $S - 2\pi a^2$ receives the horizontal infrared radiation (σT^4) emitted by the crystal environment. Hence, the total radiative flux received equals $\sigma T^4(S - 2\pi a^2) + \pi a^2(F^+ + F^-)$. Substituting (12) into the total radiative flux to eliminate $F^+ + F^-$ and then dividing the resulting expression with $\sigma T^4 S$ yields the expression of η. That is,

$$\eta - 1 = \frac{2\pi a^2}{S}(\eta_z - 1), \tag{13}$$

where S is calculated with equation (6). When $b \ll a$, $\eta \approx \eta_z$. Equation (13) quantifies Figure 2 by connecting the infrared radiation cooling/warming of ice crystals (or $\eta - 1$) to that of their air parcel (or $\eta_z - 1$).

A vertically oriented plate-like crystal is still mimicked with an oblate spheroid of semimajor and minor axis lengths a and b, but its maximum horizontal cross-sectional area becomes πab. Following the same procedure as with (13), η for a vertically oriented plate-like ice crystal is obtained, that is,

$$\eta - 1 = \frac{2\pi ab}{S}(\eta_z - 1). \tag{14}$$

Similarly, consider a bullet-shaped crystal. A horizontally (or vertically) oriented bullet-shaped crystal is mimicked by a prolate spheroid of semimajor and minor axis lengths a and b, which has a maximum horizontal cross-sectional area of πab (or πb^2). Thus,

$$\eta - 1 = \frac{2\pi ab}{S}(\eta_z - 1), \tag{15}$$

$$\eta - 1 = \frac{2\pi b^2}{S}(\eta_z - 1) \tag{16}$$

are obtained for horizontally and vertically oriented bullet-shaped crystals, respectively, where S is from equation (5).

Furthermore, the connection of η to η_z for a spherical ice crystal is obtained similarly as

$$\eta - 1 = \frac{1}{2}(\eta_z - 1). \tag{17}$$

Equations (13)–(17) can be summarized into a unifying expression or

$$\eta - 1 = \alpha(\eta_z - 1), \tag{18}$$

where the coefficient α varies with crystal size, shape, and orientation and falls between 0 and 1. For a vertically oriented ice crystal with extremely long axis ($b \ll a$), $\alpha = 0$ and thus $\eta = 1$. For a spherical crystal, $\alpha = 1/2$. For a horizontally oriented crystal with extremely long axis ($b \ll a$), $\alpha = 1$ and thus $\eta = \eta_z$.

Although the cooling (or warming) rate of an ice crystal (or $\eta - 1$) is associated with that of an air parcel (or $\eta_z - 1$) via (18), η_z and η have different applications. The ratio of an air parcel η_z is independent of ice crystals and thus is treated as a property of an air parcel. Hence, η_z can be used as a variable in cloud or climate models. In contrast, the ratio of each ice crystal η varies with α (or ice crystal shape and orientation) and, thus, is suitable for discussing the growth rate of individual ice crystals.

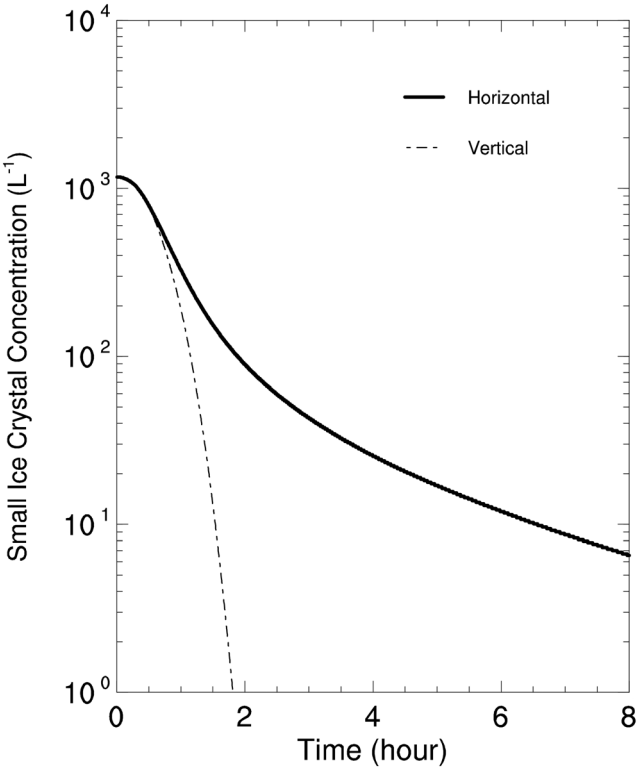

Figure 8. Concentrations of the horizontally (thick) and vertically oriented (dashed line) ice crystals whose half crystal size a is between 1 and 200 μm against time in experiment PhPv.

3. Numerical Simulations of Diamond Dust

The bin model in section 2.2 is used to simulate the effect of radiative cooling on diamond dust. Consider an air parcel with the effective vertical velocity $w_{\text{eff}} = 0$ (or approximately $w = 0$ for a stationary air parcel), $\eta_z = 0.5$ (radiative cooling) and $F_s = 0$ (no solar radiation; see section 4.1 for the effect of F_s). In this paper, seven numerical experiments are carried out to show how ice crystal properties modulate the effect of radiative cooling (see Table 2 for experiments' summary). Except for specification, all of the experiments are set up as follows: All model variables are represented in double precision. Their prognostic equations are integrated with 2,048 bins, using a time step of 0.2 s with a second-order accuracy. The air temperature $T = -30$ °C and pressure $p = 680$ hPa. The relative humidity with respect to ice is set to 100% initially. This setup mimics the environment of diamond dust observed at the South Pole Station, Antarctica (Lazzara et al., 2012; Walden et al., 2003).

3.1. Contribution of Radiative Cooling to Diamond Dust

Diamond dust involves neither riming nor aggregation (e.g., Kikuchi & Hogan, 1979; Walden et al., 2003). Thus, the bin model of diffusional growth in section 2.2 is used to simulate the effect of radiative cooling on diamond dust, where $\eta_z = 0.5$ is chosen because $\eta_z < 1$ in the arctic regions especially during wintertime (see section 4.1 for the magnitude of η_z).

The default experiment Ph addresses the evolution of horizontally oriented plate crystals. Its initial ice crystal spectrum, shown by the thick line in Figure 4, has an ICC of 2.56 cm^{-3} due to heterogeneous ice nucleation (e.g., Girard & Blanchet, 2001b) and an ice water content (IWC) of 0.8×10^{-3} g/m^3 (see section 3.4 for discussions on IWC magnitude).

If $\eta_z = 1$, the ice crystals would maintain their initial spectrum without precipitation formation. However, if $\eta_z = 0.5$, the situation changes. Figure 4 displays the modeled broadening of ice crystal spectrum with $\eta_z = 0.5$, showing that large ice crystals grow to form precipitation in a few hours. Since ice crystals with a size of 200–300 μm are treated as precipitating particles (e.g., Gultepe, 2015; Gultepe et al., 2017), Figure 4 indicates that precipitation forms in a few hours.

To show how precipitating ice crystals form, the number concentrations of ice crystals with different sizes in the experiment are analyzed. Figure 5 displays the time series of the number concentration of large (or precipitating) ice crystals whose half crystal size a is longer than 200 μm, showing an increase in the concentration of precipitating ice crystals. In contrast, the figure displays a decrease in the concentration of small ice crystals whose half crystal size a is between 1 and 200 μm (which is close to ICC). This decrease in the concentration of small ice crystals indicates the sublimation of small ice crystals, because the decrease in the concentration of small crystals far surpasses the increase in the concentration of precipitating ice crystals. Roughly speaking, when small ice crystals sublimate, some ice crystals shrink from crystal size >1 μm below 1 μm, resulting in a decrease in ICC. In summary, Figures 4 and 5 show that, when $\eta_z < 1$, large ice crystals grow whereas small ones shrink, which is consistent with the observations of Goerke et al. (2017).

The average half crystal size a for a given shape k is defined as

$$\overline{a}_k = \sum_j a M_{jk} / \sum_j M_{jk},$$

where M_{jk} represents the mass of ice crystals in a bin of j and k. Figure 6 displays the average half crystal size, IWC, and H_i against time in Ph, showing that the modeled process resembles the frost formation. When the average crystal size increases with time, REM leads to a decrease in average crystal temperature and saturation water vapor pressure around crystals. As a result, water vapor deposits on ice crystals and the environmental relative humidity (or H_i) decreases with time.

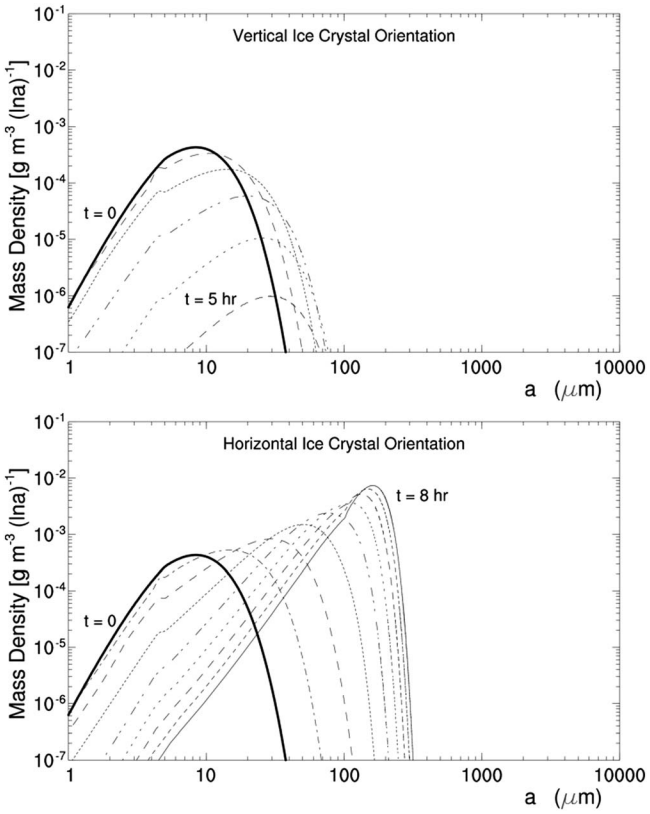

Figure 9. Same as Figure 7 except for experiment ChCv assuming column-like crystals.

3.2. Contribution to Oriented Ice Crystals

Ice crystal orientation, in addition to crystal size, is another factor to modulate REM. Two experiments, PhPv and ChCv, are carried out to show how ice crystal orientation modulates REM. PhPv represents plate crystals with two orientations. It takes the same setup as Ph except that half of its crystals are horizontally oriented and the other half are vertically oriented. Figure 7 displays the modeled spectra of vertically and horizontally oriented ice crystals, showing that the horizontally oriented ice crystals, like those in Ph, grow to form precipitating particles in a few hours. Furthermore, Figure 8 displays the concentrations of vertically and horizontally oriented ice crystals whose half crystal size is between 1 and 200 μm, showing that the vertically oriented crystals shrink due to sublimation and thus disappear quickly (Figure 7, top). In short, radiative cooling ($\eta_z < 1$) brings about lower temperatures of horizontally oriented ice crystals than those of vertically oriented ones (see Figure 3 for explanation); hence, radiative cooling favors the growth of horizontally oriented ice crystals rather than vertically oriented ones.

ChCv is carried out to model column crystals with two orientations. It takes the same setup as PhPv except for column crystals. Its modeled spectra are displayed in Figure 9, showing that radiative cooling favors horizontally oriented crystals rather than vertically oriented ones. As shown in Figures 7 and 9, plate crystals grow faster than column ones. In spite of their difference in growth rate, both PhPv and ChCv show radiative cooling favors horizontally oriented ice crystals, providing a clue to understand the formation of horizontally oriented ice crystals observed.

The dynamics of ice crystals prefers horizontal orientation of ice crystals in quiet air (e.g., Pruppacher & Klett, 1997, p. 445). Its orientation order may be disrupted by turbulence (even background one), bringing about no preferred orientation of ice crystals especially small ones (Klett, 1995; Pruppacher & Klett, 1997, p. 610). Based on the orientation model of Klett (1995) and experiments PhPv and ChCv, it is inferred that large horizontally oriented ice crystals grow from small randomly oriented ones via REM and then their orientation order remains via the ice crystal dynamics.

3.3. Selection of Ice Crystal Shape

Ice crystal habit (or shape) varies with temperature and supersaturation (e.g., Bailey & Hallett, 2009; Magono & Lee, 1966; Murray et al., 2015; see Pruppacher & Klett, 1997 for review). REM impacts crystal temperature and thus supersaturation via crystal size and shape. Thus, REM modulates ice crystal shape by selecting fast-growing crystals to survive. In this subsection, experiments PhS and PhCh are carried out to show how radiative cooling modulates ice crystal shape by selection.

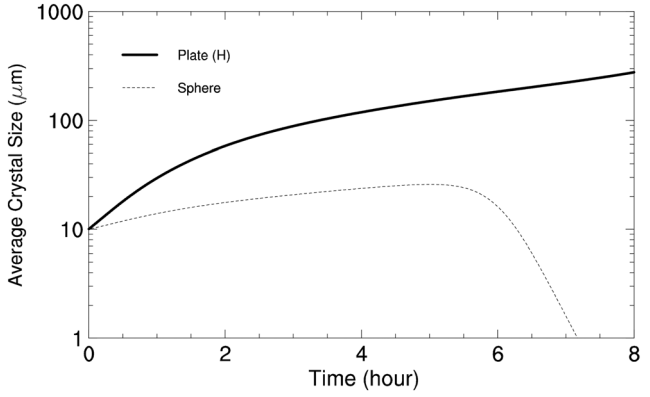

Figure 10. Average half crystal size versus time in experiment PhS. Thick and thin lines represent the average size *a* of horizontally oriented plate crystals and the average radius of spherical ice crystals, respectively.

PhS represents spherical solid ice crystals (or equidimensional ones) mixed with horizontally oriented plate ones. It takes the same setup as PhPv except that spherical crystals take the place of vertically oriented plate ones. Like those in PhPv (or Figure 7), horizontally oriented plate crystals grow to form precipitation while spherical ones disappear. Figure 10 displays the average radius of spherical ice crystals against time. The average radius increases with time first and then decreases dramatically after the plate crystals reach a size of approximately 100 μm with the emergence of dendritic extensions. These results indicate that horizontally oriented plate crystals have more chance to survive when they coexist with equidimensional ones in a stationary air parcel, which partly explains why plate/column ice crystals are common in diamond dust.

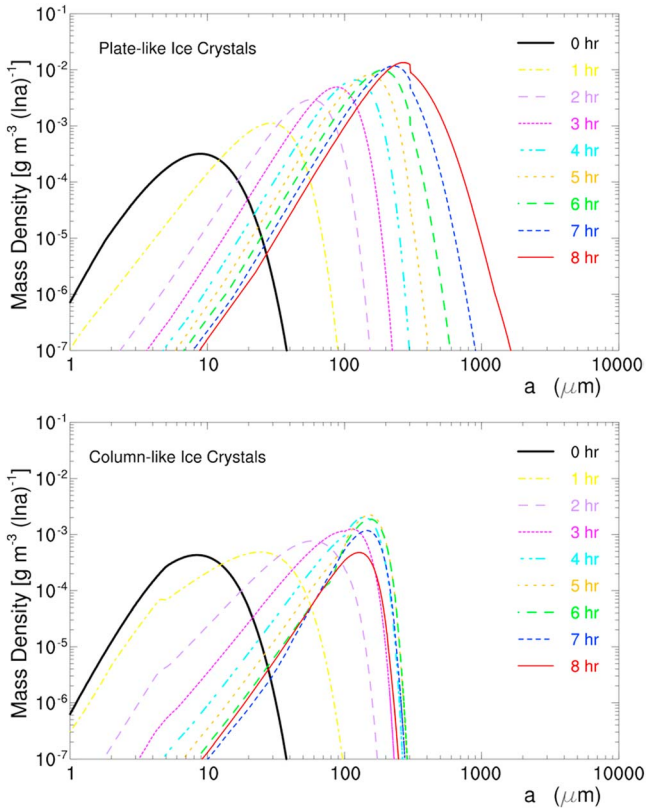

Figure 11. Same as Figure 7 except for experiment PhCh assuming horizontally oriented plate crystals (top) mixed with column ones (bottom).

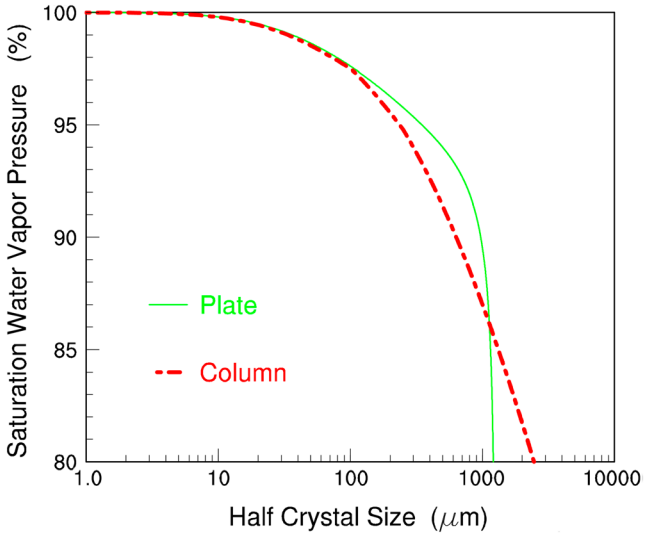

Figure 12. Saturation water vapor pressure around a plate (green) or column (red line) crystal with radiative cooling normalized by that around the same ice crystal without radiation (or the critical relative humidity) versus half crystal size a, where $\eta_z = 0.5$, $T = -30$ °C, and $p = 680$ hPa.

PhCh is carried out to model plate crystals mixed with column ones by the same number concentration, where all ice crystals are horizontally oriented. The experiment is set up the same as PhPv, except that horizontally oriented column crystals take the place of vertically oriented plate ones. Its modeling results are displayed in Figure 11. Large horizontally oriented plate and column crystals grow in expense of small plate and column ones, while the large plate crystals grow faster than the large column ones. To understand the modeling phenomenon, the saturation water vapor pressure E_i around a plate and a column crystal is displayed in Figure 12 against half crystal size a, showing that E_i around a plate crystal is close to that around a column one.

The relative humidity in PhCh decreases with time, from 100% at $t = 0$ to 96.6% at $t = 8$ hr. Based on Figure 12, it is reasoned that both plate and column crystals with half crystal size larger than 100 μm grow, which is consistent with Figure 11. The large plate crystals grow faster than the column ones, because the former have larger shape factor C than the latter. In brief, both PhS and PhCh show that radiative cooling favors plate/column ice crystals, which explains why plate and column crystals (instead of spherical or equidimensional ones) are frequently observed in diamond dust (e.g., Kikuchi & Hogan, 1979; Shimizu, 1963; Walden et al., 2003; see section 4.3 for further discussions).

3.4. Factors on Air Temperature

Three factors impact air temperature, which are (1) vertical velocity of air, (2) radiative cooling/warming of air, and (3) the conductive energy from ice crystals to air due to radiative cooling/warming of ice crystals. Since the factors impact relative humidity and subsequently ice crystal growth via air temperature, they are studied together as one factor (or the effective vertical velocity w_{eff}). In this section, experiment PhPvW is carried out to test whether the effective vertical velocity contributes to the ice crystal spectrum broadening (or the precipitation formation in diamond dust). PhPvW takes the same setup as PhPv except for an effective vertical velocity of $w_{\text{eff}} = 1$ cm/s. Figure 13 displays the modeled evolution of horizontally oriented plate crystals, and Figure 14 displays the average half crystal sizes of horizontally and vertically oriented crystals. The horizontally oriented ice crystals, like those in PhPv, grow to form precipitation in a few hours whereas the vertically oriented ones disappear in 2.5 hr, showing that vertical velocity (or radiative cooling of air) does not alter the ice crystal spectrum broadening of REM.

Figure 14 also displays the time series of IWC and crystal size in both PhPvW and PhPv, showing that the effective vertical velocity increases IWC significantly. Interestingly, the average sizes of ice crystals in PhPvW and PhPv are close to each other, which exhibits the insensitivity of ice crystal spectrum broadening to vertical velocity. These different sensitivities of IWC and crystal size to vertical velocity suggest that the radiative cooling of ice crystals, instead of vertical velocity, is the major contributor to the crystal spectrum broadening (or the precipitation formation in diamond dust) and the radiative cooling of air can effectively convert water vapor to IWC by increasing relative humidity. The sensitivities also suggest that the radiative effect can be used to overcome the modeling problem of too-narrow crystal spectrum that exists in the current cirrus models (Starr & Quante, 2002). In summary, the radiative cooling of ice crystals leads to the precipitation formation in diamond

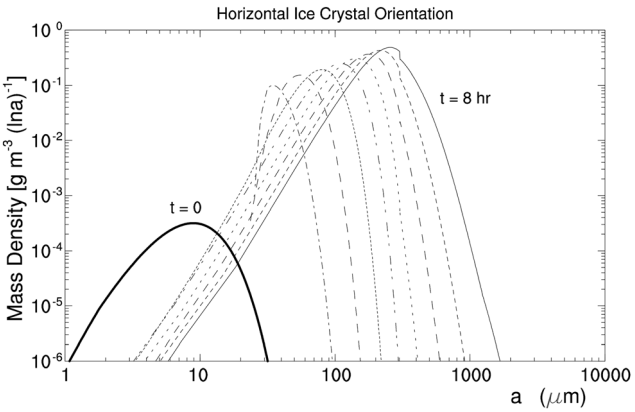

Figure 13. Evolution of horizontally oriented plate crystals in experiment PhPvW with an effective vertical velocity of 1 cm/s.

dust (or ice crystal spectrum broadening), whereas the radiative cooling of air effectively converts water vapor to IWC with little contribution to the ice crystal spectrum broadening.

3.5. Ice Crystals Falling out of Air Parcel

In the preceding experiments, ice crystals remain in the air parcel even after some of them become precipitating particles. In this section, experiment PhF is carried out to take account of the falling process: Some large ice crystals fall out of the parcel due to gravity. Consider a depth H of diamond dust. A bin of ice crystals with mass m_{jk} pass through the depth with a timescale of H/V_{jk}, where V_{jk} is the terminal velocity of ice crystal m_{jk}. Hence, the deposition of ice crystals due to gravity is described by

$$\frac{\partial m_{jk}}{\partial t} = -\frac{m_{jk}}{H/V_{jk}}.$$

Experiment PhF takes the same setup as experiment Ph except for the falling process. In the experiment, H = 1 km and the terminal velocities of ice crystals are obtained based on field observations (e.g., Auer & Veal, 1970; Heymsfield, 1972; Heymsfield & Iaquinta, 2000). Its modeled ice crystal spectra are displayed in Figure 15, where the concentration of large ice crystals is reduced significantly in comparison to that in Figure 4 so that the modeled spectra of large ice crystals are close to the observed (e.g., Kikuchi & Hogan, 1979; Walden et al., 2003).

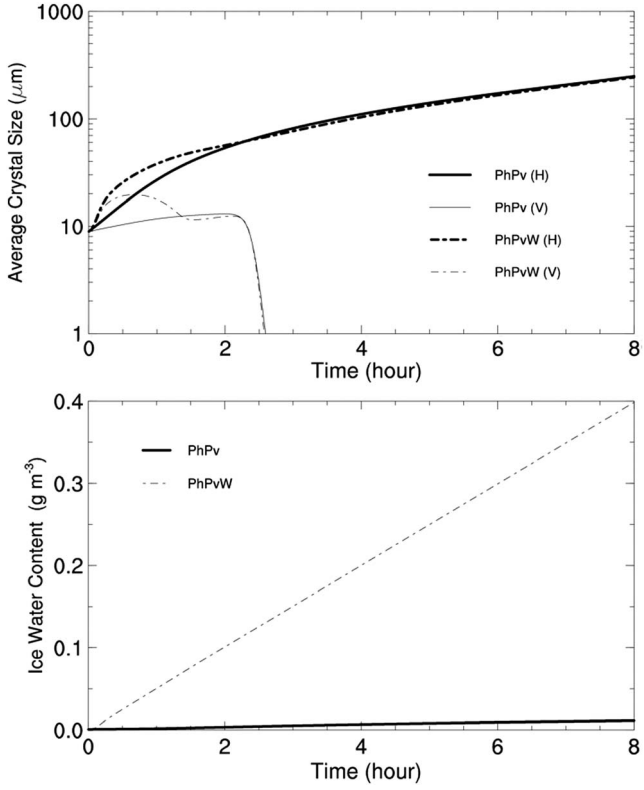

Figure 14. Time series of the average half crystal size a (top) and ice water content (bottom) in experiments PhPv (solid) and PhPvW (dashed line). Thick and thin lines in the top panel represent the average sizes of horizontally and vertically oriented plate crystals, respectively.

4. Comparison to Observations

In this section, model results are compared with observations to further analyze the contribution of radiative cooling to diamond dust.

4.1. Geographic Distribution of Diamond Dust

The geographic distribution of diamond dust can be explained by the distribution of $\eta_z - 1$ (or radiative cooling). The radiative ratio η_z varies greatly with atmospheric temperature, water vapor, sea/land surface temperature, and clouds. Since diamond dust is optically thin, it has no significant contribution to F^+ and F^- (e.g., Intrieri & Shupe, 2004). Hence, η_z in diamond dust can be computed using the atmospheric variables in clear sky.

The ratio η_z in clear sky is computed using equation (12) and the Goddard radiation package with the data of mean atmospheric states in the high latitudes (Chou et al., 1995). Its vertical profiles in winter and summer are displayed in Figure 16, showing $\eta_z < 1$ in both seasons, which indicates that the ice crystals in diamond dust undergo radiative cooling.

Since the underlying surface temperature and thus F^+ in the arctic regions are lower than those in the tropics and middle latitudes, the magnitude of η_z in the arctic regions is smaller than that in the tropics and middle latitudes (e.g., Zeng, 2008), which partly explains the high frequency of diamond dust in the arctic regions. In the interior of Antarctica, the skin temperature of snow surface is extremely low, especially in winter (e.g., the annual average temperature of −49.5 °C at South Pole Station, Lazzara et al., 2012; Figure 3 of Walden et al., 2003), which can bring about η_z much lower than that in Figure 16 and therefore the highest frequency of diamond dust there.

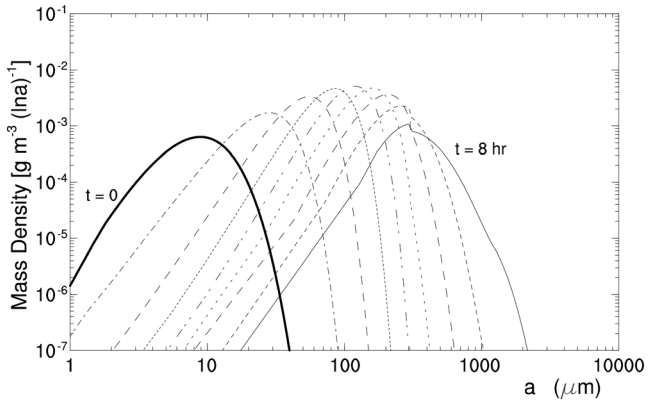

Figure 15. Same as Figure 4 except for PhF with ice crystals falling out.

Figure 16 also shows that η_z in summer is larger than that in winter, because the underlying surface temperature is higher in summer than in winter. Such difference in η_z between summer and winter partly explains why diamond dust is less frequent in summer than in late winter/early spring (Liu et al., 2012). Furthermore, solar radiation impacts diamond dust directly via REM in summer but not in winter. That is, solar radiation in summer increases ice crystal temperature and thus the effective η or

$$\eta_{\text{eff}} = \eta + F_s/\left(\varepsilon_0 \varepsilon_r \sigma T^4\right)$$

that in turn contributes to the lower frequency of diamond dust in arctic summer.

4.2. Low ICC in Diamond Dust

Radiative cooling (or $\eta_z < 1$), as shown in section 3, reinforces the growth of large ice crystals in expense of small ones, which can be used to explain the low ICC in diamond dust (e.g., Kikuchi & Hogan, 1979; Walden et al., 2003). In other words, radiative cooling can contribute much to the low ICC in diamond dust, supplementing the other mechanisms such as ice crystal falling and aggregation (e.g., Girard & Blanchet, 2001a, 2001b). Furthermore, ice nucleation is an additional factor to determine ICC and is represented in bulk by the initial ICC in the present model.

As for the connection of diamond dust to mixed-phase clouds, the low ICC may have more factors. Girard et al. (2005), for example, proposed that sulfuric acid coating on ice nuclei (IN) causes IN deactivation and thus lowers ICC. These factors for the low ICC can be tested in a complete model of diamond dust, which is beyond the scope of this paper.

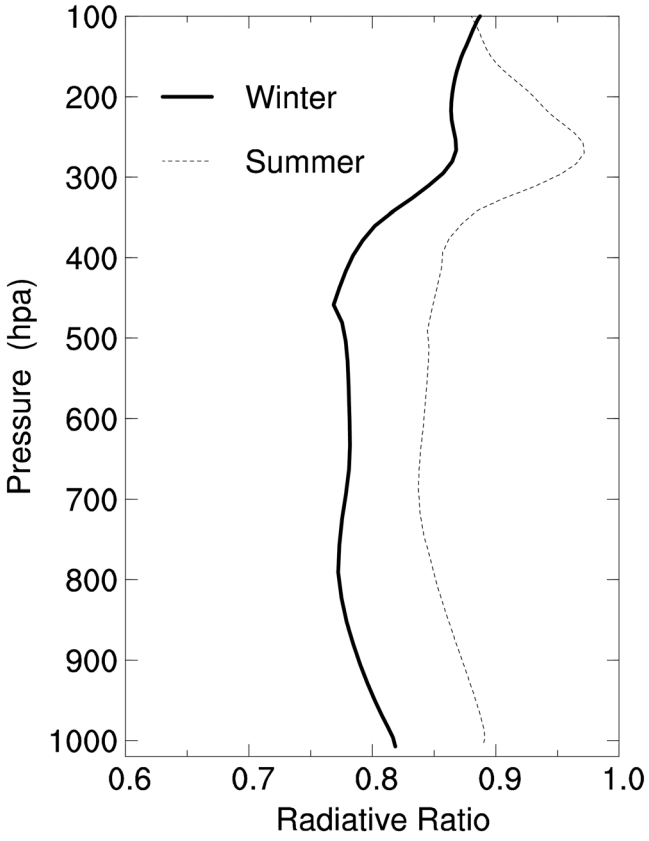

Figure 16. Vertical profiles of the radiative ratio η_z in clear sky in the high latitudes during wintertime (thick line) and summertime (thin line).

4.3. Ice Crystal Characteristics in Diamond Dust

Walden et al. (2003) observed ice crystals in diamond dust at South Pole Station, Antarctica. They found that "long prism crystals with aspect ratios greater than 5 were collected often, and very long prisms (Shimizu crystals), 1000 μm long but only 10 μm thick, were collected occasionally" and "the aspect ratio of diamond-dust ice crystals … are uncorrelated with meteorological conditions measured at the surface or within the near-surface temperature inversion." These observational results are consistent with the model prediction that large horizontally oriented column/plate-like crystals have more chance to grow than small ones or equidimensional ones. When plate- and column-like crystals with size between 100 and 1,000 μm fall through an atmospheric region with relative humidity between 86% and 97%, column-like crystals grow whereas plate-like ones sublimate (see Figure 12), which explains occasional occurrences of the Shimizu crystals. Please note that the ice crystal habit (e.g., Pruppacher & Klett, 1997) is still a major factor to determine ice crystal shape (e.g., the aspect ratio of crystal length to width) and the present model only explains the low temperature (or saturation water vapor pressure) of the Shimizu crystals due to radiative cooling.

Goerke et al. (2017) used two-dimensional reflections of a lidar beam to measure ice crystal characteristics at Summit in Greenland. They concluded "two distinct, apparently non-overlapping subpopulations of ice crystals were identified: fast precipitating snow particles … with sizes from 0.7 to 4.0 mm, and pristine ice particles consisting of smaller plates between 125 and 530 μm in size, many of which showed signs of sublimation." This discovery matches the prediction of the bin model well (e.g., experiments Ph and PhPvW) that large ice crystals grow while small ones sublimate.

Kikuchi and Hogan (1979) observed the number concentration and shape of ice crystals in diamond dust at South Pole Station, Antarctica. They

found "a time variation of two hour periodicity in the number concentration of columnar and plate type crystals" and showed "when the number concentration of columnar type crystals increased, the length of the *c*-axis of columnar type crystals also increased." This periodicity can be explained partly by a simplified bin model where ice crystals are classified into only two parts: small ice crystals (whose growth is restrained by radiative cooling; see Figure 1) and large ice crystals (whose growth is reinforced by radiative cooling). After large ice crystals fall to the ground due to gravity, small ice crystals are left aloft and then split into two parts again. Relatively larger ice crystals grow due to radiative cooling and water vapor supply by vertical mixing, becoming large ice crystals again. The large ice crystals then fall to the ground, bringing about a periodicity in ice crystal number and shape. Figure 9 shows a timescale of 2 hr for column-like crystals to grow to a crystal scale of approximately 200 μm, which is close to the variation period of ICC and shape observed by Kikuchi and Hogan (1979).

5. Conclusions

A radiation-microphysics interaction model is developed to simulate the characteristics of ice crystals in diamond dust. The model, for the first time, replicates the precipitation formation in stationary air and the low ICC of diamond dust. The model has the following features:

- Two radiative ratios, η and η_z, are introduced for an ice crystal and an air parcel, respectively. They are connected via equation (18). Since $\eta - 1$ and $\eta_z - 1$ approximately measure the radiative cooling (or warming) of an ice crystal and an air parcel, respectively, they are useful to distinguish the effect of radiative cooling from that of radiative warming on microphysics.
- A radiation-microphysics interaction model is developed to simulate the effect of radiative cooling ($\eta_z < 1$) on ice crystal properties (i.e., size, shape, and orientation). Its results show that, when $\eta_z < 1$, (1) large ice crystals grow faster than small ones, (2) horizontally oriented ice crystals grow faster than vertically oriented ones, and (3) plate-like crystals grow faster than column-like ones and the latter grow faster than equidimensional ones. Hence, when different ice crystals coexist in an air parcel to compete for available water vapor, horizontally oriented plate/column-like crystals have more chance to grow than equidimensional ones, which is consistent with the frequent observations of long-prism crystals in diamond dust (e.g., Shimizu, 1963; Walden et al., 2003).
- In an air parcel with radiative cooling (or $\eta_z < 1$), ice crystals of different sizes have different temperatures so that water vapor is saturated with respect to large ice crystals but subsaturated with respect to small ones, leading to the deposition of large ice crystals and sublimation of small ones. Such coincidence of deposition and sublimation in the model is supported by the arctic observations of Goerke et al. (2017) that large ice crystals grow whereas small ones sublimate.
- In the arctic regions, $\eta_z < 1$, which indicates that ice crystals in diamond dust undergo radiative cooling. As a result, large ice crystals—especially horizontally oriented ones—grow in expense of small ones. The geographical and seasonal distribution of $\eta_z < 1$ (or radiative cooling) can be used to explain the distribution of diamond dust, such as the most frequent diamond dust in the interior of Antarctica.

This bin model will be coupled with an atmospheric dynamic model (e.g., the eddy-resolving model in the Army Research Laboratory) to replicate the life cycle of diamond dust and ice fog, especially on the evolution of IWC and visibility.

Appendix A: Parcel Model Equations

This appendix derives the governing equations of an air parcel that undergoes radiative cooling/warming. Consider an air parcel with temperature T and water vapor pressure e. Its energy equation is expressed as

$$C_p \frac{dT}{dt} - R_d T \frac{d\ln p}{dt} = L_s \sum_{j,k} \frac{dm_{jk}}{dt} + \varepsilon_0 \sigma T^4 \sum_{j,k} S\left(\frac{F_s}{\varepsilon_0 \sigma T^4} + \varepsilon_r \eta - 1\right) + Q_r, \tag{A1}$$

where m_{jk} (j = 1, 2, ···) denotes the mass of differently sized ice crystals for a given crystal shape k, Σ denotes the summation in unit mass of dry air, the second term on the right-hand side represents the radiative energy received by ice crystals, and Q_r the radiative energy received by the gases in unit mass of dry air. For simplicity, the model (including equation (A1)) ignores the thermal capacity of water vapor and ice crystals as well as the contribution of water vapor to air pressure (see Zeng et al., 2005, for a complete treatment).

The water vapor budget of the air parcel is derived, beginning with the mixing ratio of water vapor

$$q_v = \frac{R_d}{R_v}\frac{e}{p}. \tag{A2}$$

Differentiating (A2) with respect to time gives the conservation of water vapor by

$$\frac{R_d}{R_v}\frac{e}{p}\left(\frac{\mathrm{d}e}{e\mathrm{d}t} - \frac{\mathrm{d}\ln p}{\mathrm{d}t}\right) = -\sum_{j,k}\frac{\mathrm{d}m_{jk}}{\mathrm{d}t}. \tag{A3}$$

In (A1) and (A3), $\mathrm{d}\ln p/\mathrm{d}t$ is connected to vertical velocity w via the hydrostatic equation $\mathrm{d}p/\mathrm{d}z = -\rho_a g$ and the ideal gas law $p = \rho_a R_d T$. That is,

$$\frac{\mathrm{d}\ln p}{\mathrm{d}t} = -\frac{gw}{R_d T}. \tag{A4}$$

The tendency of relativity humidity $H_i = e/E_i$ is obtained using (A1), (A3), and (A4). Differentiating H_i with respect to time, then substituting (A3) and the Clausius-Clapeyron equation into the resulting equation, and finally utilizing (A1) to remove $\mathrm{d}T/\mathrm{d}t$, giving

$$\frac{\mathrm{d}H_i}{\mathrm{d}t} = Q_1(T)w - Q_2(T)\sum_{j,k}\frac{\mathrm{d}m_{jk}}{\mathrm{d}t} + Q_3(T) \tag{A5}$$

with the aid of (A4), where

$$Q_1(T) = \frac{H_i}{T}\left[\frac{L_s g}{R_v C_p T} - \frac{g}{R_d}\right], \tag{A6}$$

$$Q_2(T) = \rho_a\left[\frac{R_v T}{E_i(T)} + \frac{R_d L_s^2 H_i}{p R_v C_p T}\right], \tag{A7}$$

$$Q_3(T) = \rho_a\frac{R_d L_s H_i}{p R_v C_p T}\left[\varepsilon_0\sigma T^4\sum_{j,k}S\left(1 - \varepsilon_r\eta - \frac{F_s}{\varepsilon_0\sigma T^4}\right) - Q_r\right]. \tag{A8}$$

When the radiative cooling/warming term Q_3 is ignored, the model of (A5)–(A8) degenerates into those of Rogers and Yau (1989) and Zeng (2008).

In (A5), the term on the left-hand side and the second term of Q_2 on the right-hand side represent the nonlinear competition of ice crystals for available water vapor, which falls into the present focus. On the other side, the first term of $Q_1(T)w$ on the right-hand side represents the contribution of vertical velocity to H_i via air temperature, which was studied well (e.g., Howell, 1949). Hence, the present discussions focus only on a given w.

The radiative term Q_3 functions similarly as vertical velocity. It changes H_i via air temperature too, without involving the competition of ice crystals for available water vapor. In this paper, it is discussed together with vertical velocity as one factor. To be specific, rewriting (A5) gives

$$\frac{\mathrm{d}H_i}{\mathrm{d}t} = Q_1(T)w_{\mathrm{eff}} - Q_2(T)\sum_{j,k}\frac{\mathrm{d}m_{jk}}{\mathrm{d}t}, \tag{A9}$$

where the effective vertical velocity is defined as

$$w_{\mathrm{eff}} = w + \frac{Q_3(T)}{Q_1(T)}. \tag{A10}$$

For a stationary air parcel (or $w = 0$), its description is equivalent to that of an air parcel with a vertical velocity of Q_3/Q_1.

The default experiment of Table 2 (or Ph) is discussed to understand its environment as an example. Since $\eta_z < 1$ (or ice crystals undergo radiative cooling), thus $Q_3 > 0$. The condition of $w_{\mathrm{eff}} = 0$ corresponds to a real vertical velocity of $w = -Q_3/Q_1 < 0$. In words, experiment Ph describes the radiatively cooled ice crystals in an air parcel with a slow subsidence.

Appendix B: List of Symbols

a/b : semimajor/minor axis length
C : stationary diffusion shape factor
C_p : specific heat of dry air
D : diffusivity of water vapor
e : partial pressure of water vapor
E_i : saturation vapor pressure over ice
f_m/f_Q : ventilation factor for mass transfer/thermal diffusion
F_s : solar flux absorbed by an ice crystal
F^+/F^- : upward/downward infrared flux
F_α/F_β : factor for the kinetic effect in heat/water vapor diffusion
g : acceleration due to gravity
$H_i = e/E_i$: relative humidity with respect to ice
H_{ic} : critical relative humidity, see equation (10)
K : coefficient of thermal conductivity of dry air
L_s : latent heat of sublimation
m : mass of an ice crystal
$M(\ln a)$: mass of ice crystals with semimajor axis length shorter than a
$N(a)$: number of ice crystals with semimajor axis length shorter than a
R_d/R_v : gas constant for dry air/water vapor
p : air pressure
r : radius of a sphere
S : surface area of an ice crystal
t : time
T : (air) temperature
w : vertical velocity
ε_0 : bulk absorption efficiency of an ice crystal for blackbody radiation
ε_r : relative bulk absorption efficiency of an ice crystal for infrared radiation
σ : the Stefan-Boltzmann constant
η : radiative ratio of an ice crystal, see equations (13)–(17)
η_z : radiative ratio of an air parcel, see equation (12)
ρ_a/ρ_v : density of air/water vapor
Δt : time step for numerical integration
ΔT : difference in temperature between ice crystal and its environmental air

Acknowledgments
The author greatly appreciated the anonymous reviewers for their critical yet constructive comments and Amber L. Bennett for reading the paper. This research was supported by the NASA Precipitation Measurement Mission (PMM) project under grant NNX16AE24G, the CloudSat/CALIPSO project under grant NNX16AM06G, and the Army Research Laboratory (ARL) Basic Research Program. The NASA Advanced Supercomputing (NAS) Division and DoD High Performance Computing (HPC) Centers provided the computer time used in this research. The model data are available at https://osf.io/4tsn3/.

References

Ackerman, A. S., Toon, O. B., & Hobbs, P. V. (1995). A model for particle microphysics, turbulent mixing and radiative transfer in the stratocumulus-topped marine boundary layer and comparisons with measurements. *Journal of the Atmospheric Sciences*, *52*(8), 1204–1236. https://doi.org/10.1175/1520-0469(1995)052<1204:AMFPMT>2.0.CO;2

Auer, A. H., & Veal, D. L. (1970). The dimension of ice crystals in natural clouds. *Journal of the Atmospheric Sciences*, *27*(6), 919–926. https://doi.org/10.1175/1520-0469(1970)027<0919:TDOICI>2.0.CO;2

Austin, P. H., Siems, S., & Wang, Y. (1995). Constraints on droplet growth in radiatively cooled stratocumulus. *Journal of Geophysical Research*, *100*, 14,231–14,242. https://doi.org/10.1029/95JD01268

Bailey, M. P., & Hallett, J. (2009). A comprehensive habit diagram for atmospheric ice crystals: Confirmation from the laboratory, AIRS II, and other field studies. *Journal of the Atmospheric Sciences*, *66*(9), 2888–2899. https://doi.org/10.1175/2009JAS2883.1

Barkstrom, B. R. (1978). Some effects of 8–12 μm radiant energy transfer on the mass and heat budgets of cloud droplets. *Journal of the Atmospheric Sciences*, *35*(4), 665–673. https://doi.org/10.1175/1520-0469(1978)035<0665:SEORET>2.0.CO;2

Bott, A., Sievers, U., & Zdunkowski, W. (1990). A radiation fog model with a detailed treatment of the interaction between radiative transfer and fog microphysics. *Journal of the Atmospheric Sciences*, *47*(18), 2153–2166. https://doi.org/10.1175/1520-0469(1990)047<2153:ARFMWA>2.0.CO;2

Brewster, Q., & McNichols, E. (2018). Measurements of radiation-induced condensational growth of cloud/mist droplets. The 98th American Meteorological Society Annual Meeting. Austin, TX.

Chou, M.-D., Ridgway, W., & Yan, M.-H. (1995). Parameterizations for water vapor IR radiative transfer in both the middle and lower atmosphere. *Journal of the Atmospheric Sciences*, *52*(8), 1159–1167. https://doi.org/10.1175/1520-0469(1995)052<1159:PFWVIR>2.0.CO;2

Curry, J. A., Schramm, J. L., Rossow, W. B., & Randall, D. (1996). Overview of Arctic cloud and radiation characteristics. *Journal of Climate*, *9*(8), 1731–1764. https://doi.org/10.1175/1520-0442(1996)009<1731:OOACAR>2.0.CO;2

Fu, Q., & Liou, K.-N. (1992). On the correlated *k*-distribution method for radiative transfer in nonhomogeneous atmospheres. *Journal of the Atmospheric Sciences*, *49*, 2153–2170.

Fuchs, N. A. (1959). *Evaporation and droplet growth in gaseous media* (p. 72). London: Pergamon Press.
Girard, E., & Blanchet, J.-P. (2001a). Microphysical parameterization of Arctic diamond dust, ice fog, and thin stratus for climate models. *Journal of the Atmospheric Sciences*, *58*, 1181–1198.
Girard, E., & Blanchet, J.-P. (2001b). Simulation of Arctic diamond dust, ice fog, and thin stratus using an explicit aerosol-cloud-radiation model. *Journal of the Atmospheric Sciences*, *58*(10), 1199–1221. https://doi.org/10.1175/1520-0469(2001)058<1199:SOADDI>2.0.CO;2
Girard, E., Blanchet, J.-P., & Dubois, Y. (2005). Effects of arctic sulphuric acid aerosols on wintertime low-level atmospheric ice crystals, humidity and temperature at Alert, Nunavut. *Atmospheric Research*, *73*(1-2), 131–148. https://doi.org/10.1016/j.atmosres.2004.08.002
Goerke, M., Ulanowski, Z., Ritter, G., Hesse, E., Neely, R. R., Taylor, L., et al. (2017). Characterizing ice particles using two-dimensional reflections of a lidar beam. *Applied Optics*, *56*(19), G188–G196. https://doi.org/10.1364/AO.56.00G188
Gong, J., Zeng, X., Wu, D. L., & Li, X. (2018). Diurnal variation of tropical ice cloud microphysics: Evidence from Global Precipitation Measurement Microwave Imager (GPM-GMI) polarimetric measurements. *Geophysical Research Letters*, *45*, 1185–1193. https://doi.org/10.1002/2017GL075519
Gultepe, I., Zhou, B., Milbrandt, J., Bott, A., Li, Y., Heymsfield, A. J., et al. (2015). A review on ice fog measurements and modeling. *Atmospheric Research*, *151*, 2–19. https://doi.org/10.1016/j.atmosres.2014.04.014
Gultepe, I., Heymsfield, A. J., Field, P. R., & Axisa, D. (2017). Ice-phase precipitation. *Meteorological Monographs*, *58*, 6.1–6.36. https://doi.org/10.1175/AMSMONOGRAPHS-D-16-0013.1
Gultepe, I., Kuhn, T., Pavolonis, M., Calvert, C., Gurka, J., Heymsfield, A. J., et al. (2018). Ice fog in Arctic during FRAM–Ice Fog Project: Aviation and nowcasting applications. *Bulletin of the American Meteorological Society*, *95*, 211–226.
Guzzi, R., & Rizzi, R. (1980). The effect of radiative exchange on the growth of a population of droplets. *Contributions to Atmospheric Physics*, *53*, 351–365.
Hall, W. D., & Pruppacher, H. R. (1976). The survival of ice particles falling from cirrus clouds in subsaturated air. *Journal of the Atmospheric Sciences*, *33*(10), 1995–2006. https://doi.org/10.1175/1520-0469(1976)033<1995:TSOIPF>2.0.CO;2
Harrington, J. Y., Feingold, G., & Cotton, W. R. (2000). Radiative impacts on the growth of a population of drops within simulated summertime Arctic stratus. *Journal of the Atmospheric Sciences*, *57*(5), 766–785. https://doi.org/10.1175/1520-0469(2000)057<0766:RIOTGO>2.0.CO;2
Heymsfield, A. (1972). Ice crystal terminal velocities. *Journal of the Atmospheric Sciences*, *29*, 1348–1357.
Heymsfield A. J. (1973). Cirrus uncinus generating cells and the evolution of cirriform clouds. Ph.D. Thesis, University of Chicago, 273 pp.
Heymsfield, A. J., & Iaquinta, J. (2000). Cirrus crystal terminal velocities. *Journal of the Atmospheric Sciences*, *57*(7), 916–938. https://doi.org/10.1175/1520-0469(2000)057<0916:CCTV>2.0.CO;2
Howell, W. E. (1949). The growth of cloud drops in uniformly cooled air. *Journal of Meteorology*, *6*(2), 134–149. https://doi.org/10.1175/1520-0469(1949)006<0134:TGOCDI>2.0.CO;2
Intrieri, J., & Shupe, M. (2004). Characteristics and radiative effects of diamond dust over the Western Arctic Ocean region. *Journal of Climate*, *17*(15), 2953–2960. https://doi.org/10.1175/1520-0442(2004)017<2953:CAREOD>2.0.CO;2
Jiang, J. H., Su, H., Zhai, C., Perun, V. S., del Genio, A., Nazarenko, L. S., et al. (2012). Evaluation of cloud and water vapor simulations in CMIP5 climate models using NASA "A-Train" satellite observations. *Journal of Geophysical Research*, *117*, D14105. https://doi.org/10.1029/2011JD017237
Kikuchi, K., & Hogan, A. W. (1979). Properties of diamond dust type ice crystals observed in summer season at Amundsen-Scott South Pole Station, Antarctica. *Journal of the Meteorological Society of Japan*, *57*(2), 180–190. https://doi.org/10.2151/jmsj1965.57.2_180
Klein, S. A., McCoy, R. B., Morrison, H., Ackerman, A. S., Avramov, A., Boer, G., et al. (2009). Intercomparison of model simulations of mixed-phase clouds observed during the ARM Mixed-Phase Arctic Cloud Experiment. I: Single-layer cloud. *Quarterly Journal of the Royal Meteorological Society*, *135*(641), 979–1002. https://doi.org/10.1002/qj.416
Klett, J. D. (1995). Orientation model for particles in turbulence. *Journal of the Atmospheric Sciences*, *52*(12), 2276–2285. https://doi.org/10.1175/1520-0469(1995)052<2276:OMFPIT>2.0.CO;2
Koeppe, C. E., & De Long, G. C. (1958). *Weather and climate* (p. 341). New York: McGraw-Hill Book Company, Inc.
Lazzara, M. A., Keller, L. M., Markle, T., & Gallaghe, J. (2012). Fifty-year Amundsen-Scott South Pole station surface climatology. *Atmospheric Research*, *118*, 240–259. https://doi.org/10.1016/j.atmosres.2012.06.027
Lebo, Z., Johnson, N., & Harrington, J. (2008). Radiative influences on ice crystal and droplet growth within mixed-phase stratus clouds. *Journal of Geophysical Research*, *113*, D09203. https://doi.org/10.1029/2007JD009262
Liu, C., & Zipser, E. J. (2009). "Warm rain" in the tropics: Seasonal and regional distributions based on 9 yr of TRMM data. *Journal of Climate*, *22*(3), 767–779. https://doi.org/10.1175/2008JCLI2641.1
Liu, Y., Key, J. R., Ackerman, S. A., Mace, G. G., & Zhang, Q. (2012). Arctic cloud macrophysical characteristics from CloudSat and CALIPSO. *Remote Sensing of Environment*, *124*, 159–173. https://doi.org/10.1016/j.rse.2012.05.006
Magono, C., & Lee, C. W. (1966). Meteorological classification of natural snow crystals. *Journal of Faculty of Science Hokkaido University*, *7*, 321–335.
Mason, B. J. (1957). *The physics of clouds* (p. 481). London: Oxford University Press.
McDonald, J. E. (1963). Use of the electrostatic analogy in studies of ice crystal growth. *Zeitschrift für Angewandte Mathematik und Physik*, *14*(5), 610–620. https://doi.org/10.1007/BF01601268
Murray, B. J., Salzmann, C. G., Heymsfield, A. J., Dobbie, S., Neely, R. R. III, & Cox, C. J. (2015). Trigonal ice crystals in Earth's atmosphere. *Bulletin of the American Meteorological Society*, *96*(9), 1519–1531. https://doi.org/10.1175/BAMS-D-13-00128.1
Powell, S. W., Houze, R. A. Jr., Kumar, A., & McFarlane, S. A. (2012). Comparison of simulated and observed continental tropical anvil clouds and their radiative heating profiles. *Journal of the Atmospheric Sciences*, *69*(9), 2662–2681. https://doi.org/10.1175/JAS-D-11-0251.1
Pruppacher, H. R., & Klett, J. D. (1997). *Microphysics of clouds and precipitation* (p. 954). Dordrecht: Kluwer.
Ricaud, P., Bazile, E., del Guasta, M., Lanconelli, C., Grigioni, P., & Mahjoub, A. (2017). Genesis of diamond dust, ice fog and thick cloud episodes observed and modelled above Dome C, Antarctica. *Atmospheric Chemistry and Physics*, *17*(8), 5221–5237. https://doi.org/10.5194/acp-17-5221-2017
Roach, W. T. (1976). On the effect of radiative exchange on the growth by condensation of a cloud or fog droplet. *Quarterly Journal of the Royal Meteorological Society*, *102*(432), 361–372. https://doi.org/10.1002/qj.49710243207
Rogers, R. R., & Yau, M. K. (1989). *A short course in cloud physics* (3rd ed., p. 290). Oxford: Butterworth-Heinemann.
Santachiara, G., Belosi, F., & Prodi, F. (2017). Ice crystal precipitation at Dome C site (East Antarctica). *Atmospheric Research*, *167*, 108–117.
Shimizu, H. (1963). "Long prism" crystals observed in the precipitation in Antarctica. *Journal of the Meteorological Society of Japan*, *41*(5), 305–307. https://doi.org/10.2151/jmsj1923.41.5_305
Skofronick-Jackson, G., Heymsfield, A., Holthaus, E., Albers, C., & Kim, M.-J. (2008). Nonspherical and spherical characterization of ice in Hurricane Erin for wideband passive microwave comparisons. *Journal of Geophysical Research*, *113*, D06201. https://doi.org/10.1029/2007JD008866

Skofronick-Jackson, G., Hudak, D., Petersen, W., Nesbitt, S. W., Chandrasekar, V., Durden, S., et al. (2015). Global Precipitation Measurement Cold Season Precipitation Experiment (GCPEX): For measurement's sake, let it snow. *Bulletin of the American Meteorological Society*, *96*(10), 1719–1741. https://doi.org/10.1175/BAMS-D-13-00262.1

Small, J. D., & Chuang, P. Y. (2008). New observations of precipitation initiation in warm cumulus clouds. *Journal of the Atmospheric Sciences*, *65*(9), 2972–2982. https://doi.org/10.1175/2008JAS2600.1

Starr, D. O., & Quante, M. (2002). Dynamical processes in cirrus clouds. In D. K. Lynch, K. Sassen, D.O'C. Starr, & G. Stephens (Eds.), *Cirrus* (pp. 256–264). New York: Oxford University Press.

Stephens, G. L. (1983). The influence of radiative transfer on the mass and heat budgets of ice crystals falling in the atmosphere. *Journal of the Atmospheric Sciences*, *40*(7), 1729–1739. https://doi.org/10.1175/1520-0469(1983)040<1729:TIORTO>2.0.CO;2

van As, D., & van den Broeke, M. R. (2006). Structure and dynamics of the summertime atmospheric boundary layer over the Antarctic Plateau: 2. Heat, moisture, and momentum budgets. *Journal of Geophysical Research*, *111*, D07103. https://doi.org/10.1029/2005JD006956

Walden, V. P., Warren, S. G., & Tuttle, E. (2003). Atmospheric ice crystals over the Antarctic Plateau in winter. *Journal of Applied Meteorology*, *42*(10), 1391–1405. https://doi.org/10.1175/1520-0450(2003)042<1391:AICOTA>2.0.CO;2

Warren, S. G., & Brandt, R. E. (2008). Optical constants of ice from the ultraviolet to the microwave: A revised compilation. *Journal of Geophysical Research*, *113*, D14220. https://doi.org/10.1029/2007JD009744

Wu, T., Cotton, W. R., & Cheng, W. Y. Y. (2000). Radiative effects on the diffusional growth of ice particles in cirrus clouds. *Journal of the Atmospheric Sciences*, *57*(17), 2892–2904. https://doi.org/10.1175/1520-0469(2000)057<2892:REOTDG>2.0.CO;2

Zeng, X. (2008). The influence of radiation on ice crystal spectrum in the upper troposphere. *Quarterly Journal of the Royal Meteorological Society*, *134*(632), 609–620. https://doi.org/10.1002/qj.226

Zeng, X. (2018a). Modeling the effect of radiation on warm rain initiation. *Journal of Geophysical Research : Atmospheres*, *123*, 6896–6906. https://doi.org/10.1029/2018JD028354

Zeng, X. (2018b). *Using CloudSat and GMI data to identify the radiative effect on cloud microphysics* (pp. 23–25). Boulder, CO: The 2018 CloudSat/CALIPSO Annual Science Review.

Zeng, X., Skofronick-Jackson, G., Tian, L., Emory, A. E., Olson, W. S., & Kroodsma, R. A. (2016). *Analysis of the GMI/CoSMIR microwave polarization data for ice crystal modeling*, (pp. 24–28). Houston, Texas: The 2016 Precipitation Measurement Mission (PMM) meeting.

Zeng, X., Tao, W.-K., Powell, S. W., Houze, R. A. Jr., Ciesielski, P., Guy, N., et al. (2013). A comparison of the water budgets between clouds from AMMA and TWP-ICE. *Journal of the Atmospheric Sciences*, *70*(2), 487–503. https://doi.org/10.1175/JAS-D-12-050.1

Zeng, X., Tao, W.-K., & Simpson, J. (2005). An equation for moist entropy in a precipitating and icy atmosphere. *Journal of the Atmospheric Sciences*, *62*(12), 4293–4309. https://doi.org/10.1175/JAS3570.1

Zhang, M. H., Lin, J. L., Cederwall, R. T., Yio, J. J., & Xie, S. C. (2001). Objective analysis of ARM IOP data: Method and sensitivity. *Monthly Weather Review*, *129*(2), 295–311. https://doi.org/10.1175/1520-0493(2001)129<0295:OAOAID>2.0.CO;2